













# Evolution of a long-period Cataclysmic Variable from the viewpoint of the donor star: the case of SDSS J085210.48+783246.6

G. Tovmassian <sup>1,2</sup>, \* D. Belloni <sup>3</sup>, I. Mora Zamora <sup>4</sup>, B.T. Gänsicke <sup>5</sup>, S. Zharikov <sup>1</sup>,  
J. Echevarria <sup>4</sup>, M.R. Schreiber <sup>6</sup>, P. D’Avanzo <sup>2</sup>, P. Ochner <sup>7,8</sup>, R. Ashley <sup>5</sup> and K. Inight <sup>5</sup>

<sup>1</sup>Universidad Nacional Autónoma de México. Instituto de Astronomía. A.P. 106, 22800. Ensenada, B.C., México

<sup>2</sup>INAF – Osservatorio Astronomico di Brera, Via E. Bianchi 46, 23807 Merate (LC), Italy

<sup>3</sup>International Centre of Supernovae (ICESUN), Yunnan Key Laboratory of Supernova Research, Yunnan Observatories, Chinese Academy of Sciences (CAS), Kunming 650214, China

<sup>4</sup>Universidad Nacional Autónoma de México. Instituto de Astronomía. A.P. 70-264, 04510. Ciudad de México, México

<sup>5</sup>Department of Physics, University of Warwick, Coventry, CV4 7AL, UK

<sup>6</sup>Departamento de Física, Universidad Técnica Federico Santa María, Av. España 1680, Valparaíso, Chile

<sup>7</sup>Università degli Studi di Padova, Dipartimento di Fisica e Astronomia, Vicolo dell’Osservatorio 3, 35122 Padova, Italy

<sup>8</sup>INAF – Osservatorio Astronomico di Padova, Vicolo dell’Osservatorio 5, I-35122 Padova, Italy

Accepted XXX. Received YYY; in original form ZZZ

## ABSTRACT

Cataclysmic variables were long considered to be close binaries consisting of a white dwarf and a Roche-lobe-filling, near-zero-age main-sequence (ZAMS) red or brown dwarf. Recent massive surveys have uncovered an increasing number of binaries with similar spectral characteristics but harboring secondary stars that have undergone nuclear evolution and partial envelope stripping, many with orbital periods far exceeding the normal upper limits for ordinary CVs. We present a detailed study of a newly discovered CV with a 17.109 h period and determine its basic stellar parameters. We also discuss the evolutionary paths leading to the formation of these extremely long-period cataclysmic variables. We consider the implications of the new evolutionary hypothesis on their further evolution into double-degenerate binaries.

**Key words:** cataclysmic variables — binaries: close — stars: evolution — accretion, accretion discs — white dwarfs — stars: individual: SDSS J085210.48+783246.6

## 1 INTRODUCTION

In cataclysmic variables (CVs), close binary systems in which a white dwarf accretes from a main-sequence or slightly evolved donor star, the evolution proceeds from longer towards shorter orbital periods, driven mainly by magnetically guided winds carrying away angular momentum in a mechanism known as magnetic wind braking at periods above 3 h and by gravitational waves at shorter periods (e.g. Knigge et al. 2011; Belloni & Schreiber 2023). For decades, the evolution of CVs has been modelled under the assumption of magnetic braking prescriptions derived from the spin-down of slowly rotating sun-like stars (Skumanich 1972). The resulting prescription predicts a strong dependence of angular momentum loss on the spin period (Rappaport et al. 1983), and the corresponding evolutionary models are still considered the standard scenario for CV evolution.

However, there is growing evidence that this standard prescription for magnetic braking is significantly flawed. Observational and theoretical studies of fast-rotating low-mass stars have established that the magnetic braking torque saturates for spin periods shorter than a certain threshold; that is, the dependence of angular momentum loss on rotation rate becomes much shallower than predicted by Rappaport et al. (1983) (e.g. Barnes & Sofia 1996; Reiners & Mohanty

2012; Matt et al. 2015). El-Badry et al. (2021) showed that this saturation is also relevant in close binaries with evolved donors, and that the standard prescription consequently overestimates angular momentum loss in such systems. Revised prescriptions that incorporate saturation have been successfully applied to CVs (Barraza-Jorquera et al. 2025) and their progenitors (Belloni et al. 2024).

Perhaps most importantly, Belloni & Schreiber (2023) showed that more efficient angular-momentum loss via magnetic braking in slightly evolved donors can solve long-standing problems in the formation of ultra-compact binaries from CVs. Under this picture, CVs with evolved donors and unusually long periods are the natural progenitors of extremely low-mass white dwarfs with more massive companions (El-Badry et al. 2021; Aros-Bunster et al. 2025; Belloni et al. 2025). These in turn may evolve into AM CVn systems, short-period ( $\lesssim 60$  min) binaries in which a white dwarf accretes from a helium-dominated donor (Belloni & Schreiber 2023). The prescription of Van & Ivanova (2019), and the even stronger braking scenarios explored by Sarkar et al. (2023a,b), provide the angular-momentum loss rates required to connect these systems within a single evolutionary sequence. The previously termed paradoxical double white dwarf binaries (Aros-Bunster et al. 2025; Belloni et al. 2025) fit naturally into this sequence as descendants of mass-transferring and recently detached CVs with evolved secondaries (El-Badry et al. 2021).

If the scenario just outlined is correct, the properties of CVs with

\* E-mail: gag@astro.unam.mx

evolved donors and longer orbital periods, corresponding to an earlier stage of the same evolutionary sequence, should be explicable under strong magnetic braking, as proposed by [Van & Ivanova \(2019\)](#). Recently, [Tovmassian et al. \(2025\)](#) showed that two long-period CVs, V479 And and V1082 Sgr, can indeed be explained as extremely long-period CVs with nuclear-evolved donors if such strong magnetic braking is assumed. Long-period CVs with evolved donors are not entirely new phenomena: GK Per (Nova Persei 1901), with an orbital period of  $\sim 48$  h and an undermassive subgiant donor ([Álvarez-Hernández et al. 2021](#)), has long stood as an outstanding, but poorly understood example of this class. Recent massive surveys, however, have uncovered an increasing number of such systems, which we explore.

In this paper, we extend this investigation to SDSS J085210.48+783246.6 (hereinafter SDSS J0852+7832), an eclipsing long-period CV whose fundamental parameters we derive and interpret within the same framework, showing that it is best understood as a progenitor of V479 And at an earlier stage of the sequence.

## 2 COMPREHENSIVE STUDY OF SDSS J0852+7832

SDSS J0852+7832 was identified as a CV candidate in a project that used machine learning on *GALEX* (*FUV*, *NUV*) and *Gaia* (*G*,  $G_{BP}$ ,  $G_{RP}$ ) absolute magnitudes plus an aggregate *Gaia*-based variability metric (see Eq. 1 of [Guidry et al. 2021](#)). We trained a Random Forest Classifier using 1200 spectroscopically confirmed CVs ([Ritter & Kolb 2003](#); [Szkody et al. 2011](#)) as a training sample. Full details on the about 200 CV candidates identified in this project will be discussed elsewhere.

The eclipsing nature of SDSS J0852+7832 and its very long orbital period of about 17 h was determined from the analysis of the ZTF photometry ([Bellm et al. 2019](#)), and its CV nature was confirmed by spectroscopy obtained at the Isaac Newton Telescope (see below). *Gaia* determines a parallax of  $p = 0.9180 \pm 0.0159$  mas corresponding to a distance  $D = 1108.3^{+19.2}_{-18.5}$  pc ([Gaia Collaboration et al. 2023](#)). [Bailer-Jones et al. \(2021\)](#) calculates a slightly smaller distance of  $1053^{+17}_{-19}$  pc. Throughout this work, we adopt the [Bailer-Jones et al. \(2021\)](#) distance, which incorporates a probabilistic prior on the Galactic stellar density distribution and is more robust than simple parallax inversion at this moderate signal-to-noise ratio.

### 2.1 Observations

We acquired spectrophotometric observations of SDSS J0852+7832 and complemented them with publicly available photometric data from ground-based and satellite telescopes.

#### 2.1.1 Spectrophotometry

SDSS J0852+7832 was observed spectroscopically by the Sloan Digital Sky Survey V (SDSS-V) as part of its multi-epoch spectroscopic monitoring program. Three optical spectra were obtained using the BOSS spectrograph on the Apache Point Observatory 2.5 m telescope ([Smee et al. 2013](#)). The BOSS spectrograph delivers a spectral resolution of  $R \approx 2000$  over the wavelength range about 3600 to 10400 Å.

The observations were carried out on Modified Julian Dates (MJDs) 59651, 59653, and 59654 which we denote as spectra #51, #53, and #54, providing consecutive nightly coverage. The spectra differ markedly from one another, and, as we found using the system

ephemeris (see Section 3.1), spectrum #54 was obtained during the eclipse and reveals prominent absorption features of the secondary star. In contrast to #54, spectra #53 and #51 demonstrate strong Balmer, He I, and He II emission lines typical for CVs. The spectrum #53 was obtained at the maximum brightness of the system. In Fig. 1 we present spectra #53 and #54. The major emission lines are marked. We omit the intermediary spectrum #51 for clarity.

Phase-resolved observations of SDSS J0852+7832 were obtained with the Intermediate Dispersion Spectrograph (IDS) mounted on the 2.54 m Isaac Newton Telescope (INT) at the Observatorio del Roque de los Muchachos, La Palma. We used the R632V grating centred at 5720 Å, providing a spectral coverage from 4383 to 6704 Å at a dispersion of  $0.89 \text{ \AA pixel}^{-1}$ . A total of 60 exposures of 600 s each (10 h total integration) were collected between 2020 February 10 and 20. All spectra were optimally extracted and reduced using the PAMELA and MOLLY packages ([Marsh 1989](#)). Wavelength calibration was performed using Cu+Ne and Cu+Ar comparison lamps taken at the start and end of each night and approximately once per hour during the longer observing sequences. As a final refinement, we measured the position of the telluric O I  $\lambda 5577.4 \text{ \AA}$  emission line in the sky spectrum and corrected any residual wavelength offsets to match its laboratory value. The INT spectra were not flux-calibrated.

Complementary observations were carried out with the 1.22 m telescope at the Asiago Observatory equipped with the Boller & Chivens spectrograph and an ANDOR iDus DU440A E2V 42-10 back-illuminated CCD. Observations took place between 2024 January 21 and 23, yielding fifty long-slit spectra evenly distributed over the orbital cycle. These spectra were obtained with a  $12001 \text{ mm}^{-1}$  grating, providing a reciprocal dispersion of  $0.6 \text{ \AA pixel}^{-1}$  and a resolving power of about  $2.3 \text{ \AA}$  (FWHM) over the 4580 to 5820 Å range. An additional set of sixteen spectra was secured on 2024 February 1 using a  $6001 \text{ mm}^{-1}$  grating, covering 4250 to 6590 Å with a  $4.5 \text{ \AA}$  FWHM resolution.

All Asiago data were reduced following standard long-slit spectroscopy procedures in IRAF<sup>1</sup>, including bias subtraction, flat-field correction, and wavelength calibration using He+Ar arc-lamp exposures obtained contemporaneously with the science frames. Flux calibration was achieved with the spectrophotometric standard stars HR 4554 and HR 5501 observed on the same nights.

#### 2.1.2 Photometry

All-sky monitoring telescopes, including the All-Sky Automated Survey for Supernovae (ASAS-SN; [Shappee et al. 2014](#); [Kochanek et al. 2017](#)), Zwicky Transient Facility (ZTF; [Bellm et al. 2019](#)), Asteroid Terrestrial-impact Last Alert System (ATLAS; [Heinze et al. 2018](#)) and Transiting Exoplanet Survey Satellite ([Ricker et al. 2015](#)) data have covered the object at different epochs and with a variety of filters. A summary of sky-patrol observations is presented in Table 1.

TESS observed the SDSS J0852+7832 on 2021-06-25 through 07-23, 2021-12-31 through 2022-01-07; 2022-06-13 through 07-08, and 2022-12-23 through 2023-01-18 with a standard cadence of 120 s. We specifically used the light curves provided by the TESS Science Processing Operations Center (SPOC<sup>2</sup> [Jenkins et al. 2016](#)) through

<sup>1</sup> IRAF (Image Reduction and Analysis Facility) is distributed by the National Optical Astronomy Observatory, which is operated by the Association of Universities for Research in Astronomy (AURA) under a cooperative agreement with the National Science Foundation.

<sup>2</sup> <https://archive.stsci.edu/hlsp/tess-spoc>

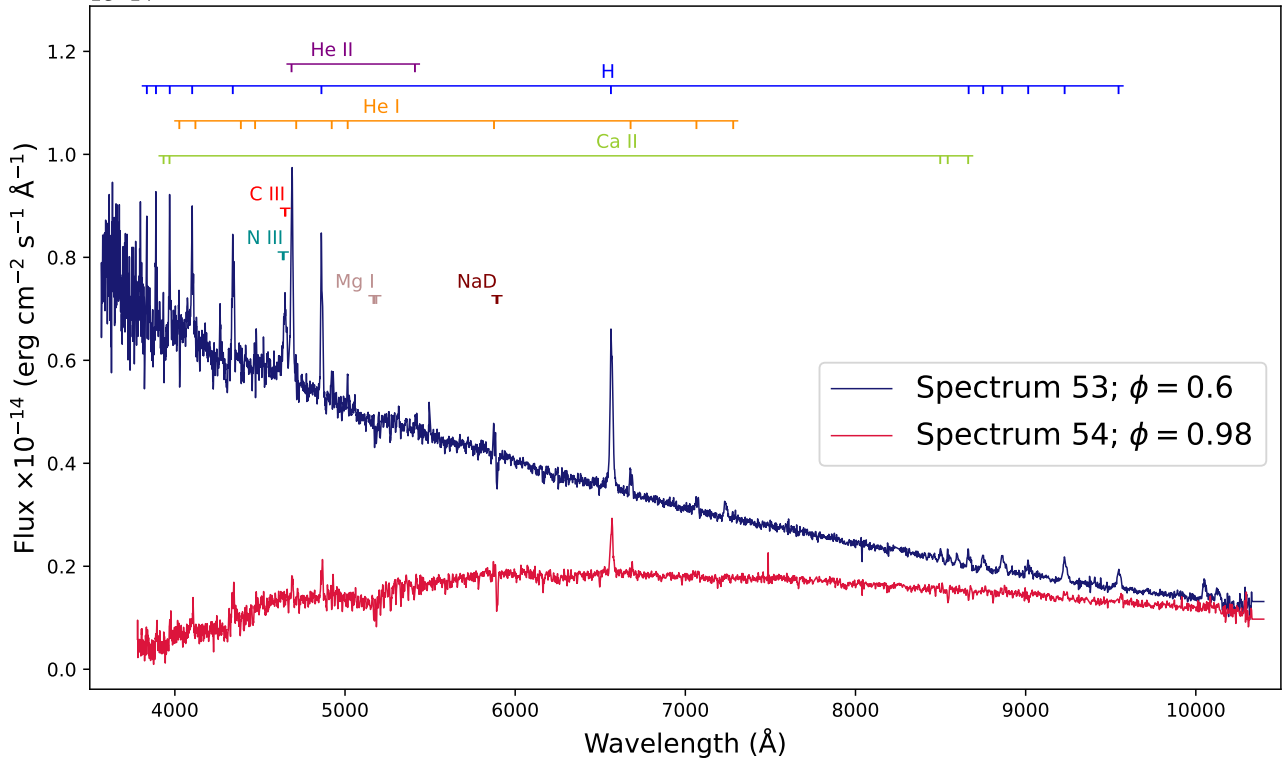


**Figure 1.** SDSS BOSS spectra of SDSS J0852+7832 obtained during the bright phase (blue) and during eclipse (red). The spectra are shown in absolute flux units. The reduced flux level of spectrum #54 reflects its acquisition during eclipse.

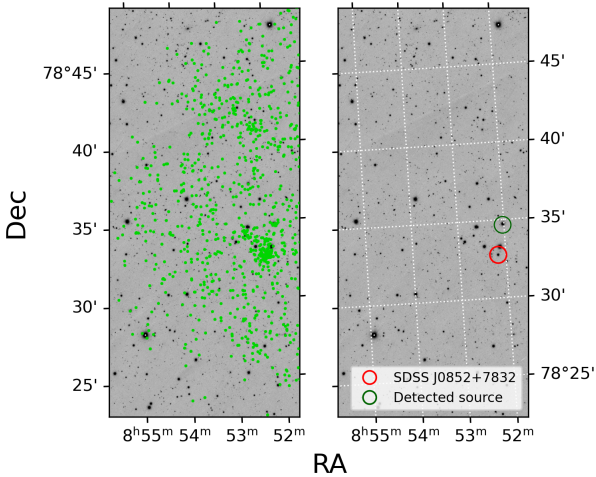


**Figure 2.** The image of SDSS J0852+7832 in PanSTARRS  $i$ -band with overlaid *Swift* XRT X-ray detection map (left panel). In the right panel, just the optical image is repeated with the SDSS J0852+7832 marked in addition to a randomly detected point source in this piece of sky.

the Barbara A. Mikulski Archive for Space Telescopes (MAST<sup>3</sup>), and the PDCSAP flux, which corrects an initial simple aperture photometry (SAP) to remove instrumental trends and contributions from neighbouring stars using pre-search data conditioning. Nevertheless, examination of the TESS light curves shows negligible flux variability from epoch to epoch but more significant (about 0.35 mag)

<sup>3</sup> <https://archive.stsci.edu/missions-and-data/teess>

divergence at the bottom of the eclipse. The reason is not clear, but it can be mitigated by relying on multi-epoch, multi-colour observations from all-sky patrol missions, where no such large differences in the eclipse depth are observed.

### 2.1.3 *Swift* UV and X-ray observations

*Swift* (Gehrels et al. 2004) observed SDSS J0852+7832 upon our request (Target ID 165180). Ten exposures were distributed around the orbital phases to cover the entire orbital period. However, a gyroscope failure on board the spacecraft reduced the number of usable exposures; only four images of sufficient quality were obtained with the UVM2 filter on the UVOT telescope (Roming et al. 2005). This is insufficient to analyse the light curve. However, we measured the average flux outside the eclipse.

On the other hand, *Swift*/XRT (Burrows et al. 2000) shows a very low signal in each of the  $\approx 1000$  s snapshots. In the combined 0.3 to 10 keV image, our target appears as a diffuse concentration of photons, distinguishable but not cleanly point-like. Fig. 2 displays the Pan-STARRS map (Flewelling et al. 2020) with the X-ray events overlaid; for clarity, we repeat the optical image (right panel) and mark the positions of SDSS J0852+7832 and a nearby star (Pul-3 500095), the latter detected as a reasonably strong X-ray source. At the optical position of SDSS J0852+7832 we measure a PC-mode count rate of  $(3.7 \pm 0.9) \times 10^{-3}$  ct s<sup>-1</sup> in 0.2 to 10 keV, extracted with a standard 20-pixel (47'') circular aperture, which encloses 90% of the PSF at 1.5 keV; the ARF from *xrtmkarf* applies the encircled-energy correction (Capaldi et al. 2005). The background was estimated from a concentric, source-masked annulus with inner/outer radii of 40/80 pixels (94'' to 188''), with exposure-map weighting applied to both source and background regions to correct

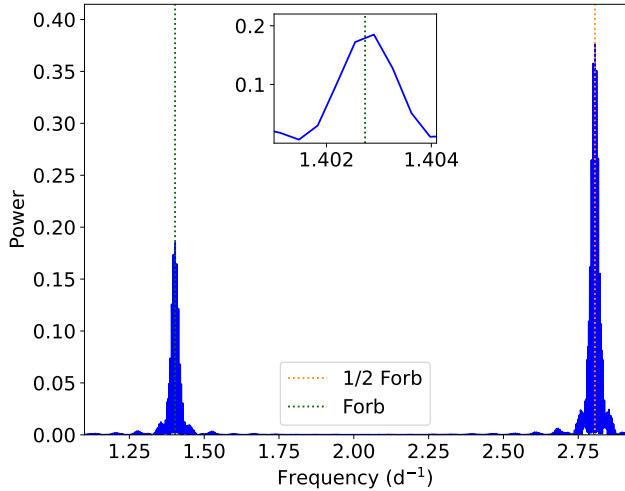


**Figure 3.** The power spectrum of the combined photometric time series (TESS, ZTF, ASASSn, and Atlas). Two peaks correspond to frequencies of strong periodic variability corresponding to the orbital period and half of the orbital period, as a consequence of the double-humped light curve. The power is shown in normalized, dimensionless units.

for vignetting and bad pixels. For the count-to-flux conversion we adopt an absorbed thermal bremsstrahlung model, `tbabs*bremss`, with  $kT = 7$  keV and a Galactic column  $N_{\text{H}} = 2 \times 10^{20} \text{ cm}^{-2}$  from the HI4PI map (HI4PI Collaboration 2016); this choice is appropriate for post-shock emission in accreting magnetic white dwarfs and reproduces the observed hardness within the uncertainties. The resulting unabsorbed on-axis flux is  $(1.6 \pm 0.4) \times 10^{-13} \text{ erg cm}^{-2} \text{ s}^{-1}$  in 0.2–10 keV. Although many XRT analyses quote 0.3 to 10 keV because of low-energy calibration systematics, the difference is immaterial at such low  $N_{\text{H}}$  (Godet et al. 2009). Adopting the distance used throughout this work,  $d = 1053^{+17}_{-19} \text{ pc}$ , we obtain  $L_X = (2.12 \pm 0.52_{\text{stat}} \pm 0.07_{\text{dist}}) \times 10^{31} \text{ erg s}^{-1}$  via  $L = 4\pi d^2 F$  (Burrows et al. 2005; Capalbi et al. 2005; HI4PI Collaboration 2016; UK Swift Science Data Centre 2023). An additional systematic uncertainty of comparable magnitude arises from the assumed spectral model; this does not affect our conclusions.

### 3 SYSTEM PARAMETERS

From the observed photometric and spectroscopic data, we derive the fundamental parameters of the binary system. These parameters form the basis for the subsequent analysis of its physical properties and evolutionary status.

#### 3.1 Orbital period and ephemeris

A Lomb–Scargle periodogram (Fig. 3) computed from the detrended TESS light curve shows a dominant frequency at  $1.4020(1) \text{ d}^{-1}$ , corresponding to  $P = 0.7129(1) \text{ d}$  (17.11 h), which we identify as the orbital period. A secondary peak at twice this frequency reflects the ellipsoidal modulation of the donor star. The absence of significant aliases confirms that the period is unambiguously determined.

To refine the ephemeris, we measured the times of mid-eclipse by fitting Gaussian profiles to the minima in both the TESS and ground-based light curves, using data within orbital phases  $-0.35$  to  $+0.35$ . This also allowed us to estimate the magnitude in the eclipse and its depth in different filters. All timestamps were converted to the

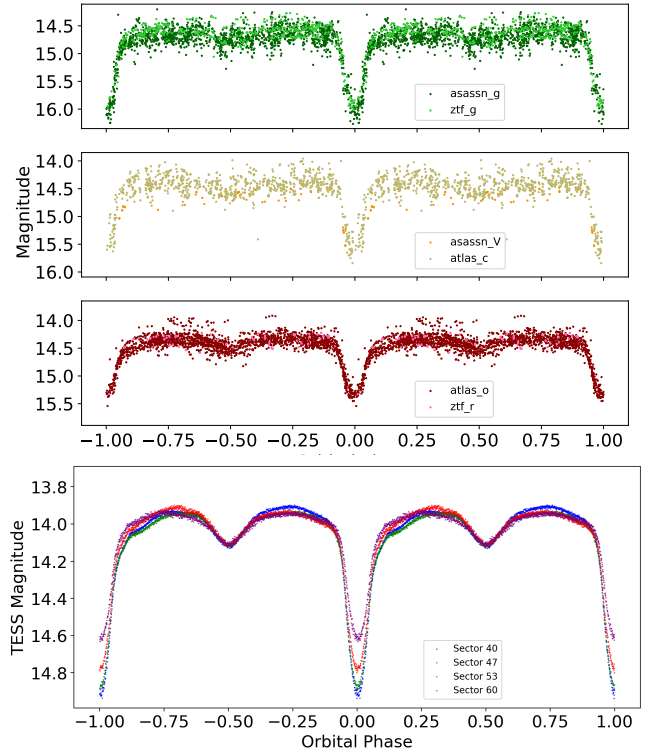


**Figure 4.** The light curve of SDSS J0852+7832 in different bands collected by different sky patrol surveys (indicated in the legend) and folded with the orbital period is presented in the upper panel. In the lower panel, a binned TESS light curve is shown as points of different colours, corresponding to different epochs, marked by sector numbers in the legend. The overall brightness varies slightly from epoch to epoch; therefore, we have adjusted them to the same magnitude at phase 0.5 in Sector 53. While the shape of the TESS light curve is very definite, the depths of eclipses are not.

barycentric dynamical time system ( $\text{BJD}_{\text{TDB}}$ ). A linear least-squares fit to the resulting eclipse timings yields:

$$T_{\text{mid}}(\text{BJD}_{\text{TDB}}) = 2458909.043(2) + 0.712892376(5) E, \quad (1)$$

where  $E$  is the orbital cycle number,  $T_0 = 2458909.043(2)$  corresponds to the time of mid-primary eclipse, and  $P_{\text{orb}} = 0.712892376(5) \text{ d}$  is the refined orbital period. No significant departure from a linear trend is detected in the observed minus calculated (O–C) residuals listed in Table 1. In Fig. 4, we present folded with the orbital period the available data from all surveys and TESS.

#### 3.2 Donor Star Spectrum Fitting and $\chi^2$ Minimization

To constrain the physical properties of the donor star in SDSS J0852+7832, we performed a detailed spectral energy distribution (SED) fitting using a grid of BT-Settl synthetic spectra<sup>4</sup> (Allard 2014). BT-Settl models incorporate detailed molecular opacities, dust formation, and convection, making them particularly well-suited for representing the atmospheres of cool stars with complex chemistry. The model grid we used spans a wide range of effective temperatures (4200–5000 K, in 100 K steps) and surface gravities

<sup>4</sup> <https://phoenix.ens-lyon.fr/Grids/BT-Settl/AGSS2009/>

**Table 1.** Eclipse depth, minimum magnitude, and O–C residuals for different surveys.

Survey	Eclipse depth (mag)	Min. magnitude	O–C (d)	No. Points	No. orbital cycles
ASAS-SN ( <i>g</i> )	−1.438	16.13	0.000	1520	3193
ZTF ( <i>g</i> )	−1.718	16.49	−0.002	53	1227
ASAS-SN ( <i>V</i> )	−1.189	15.63	−0.003	836	3473
ATLAS ( <i>c</i> )	−1.365	15.99	−0.001	466	4191
ATLAS ( <i>o</i> )	−0.996	15.40	0.000	1795	4218
ZTF ( <i>r</i> )	−0.995	15.35	0.003	89	1260

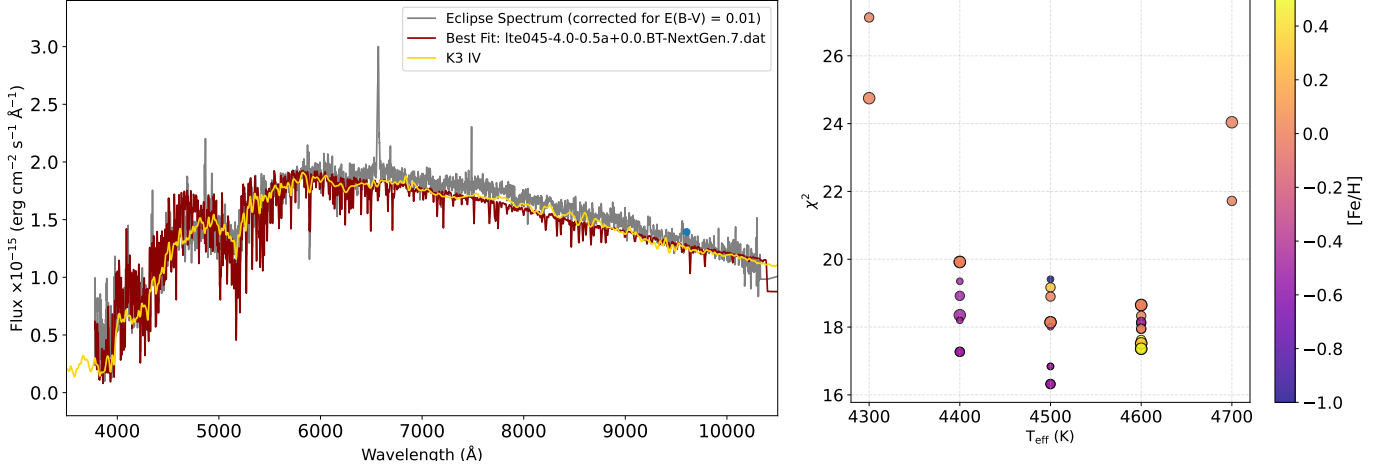


**Figure 5.** Left: Observed SDSS spectrum during eclipse, corrected for interstellar extinction (grey). The best-fit composite model (BT-Settl) is shown in dark red. The blue point indicates NIR photometric data; the rest are not shown in this figure but were included in the fitting. Right: Reduced  $\chi^2$  for BT-Settl models in the grid considered during the fitting. Marker colour indicates effective temperatures, and size is scaled with  $\log g$ ; larger circles correspond to  $\log g$  ( $\text{cm s}^{-2}$ ) = 3.5, smaller to 4.5. A negative metallicity slightly improves the fit at lower temperatures, whereas a positive metallicity slightly improves it at higher temperatures. For solar abundances, the best fit is between 4500 and 4600 K. This diagnostic helps visualize the temperature–gravity region favoured by the observed spectrum. The formal best fit is achieved for  $T_{\text{eff}} = 4500$  K,  $\log g$  ( $\text{cm s}^{-2}$ ) = 4.0,  $R = 1.40 R_{\odot}$ , and  $D = 1073$  pc.

( $3.5 < \log g$  ( $\text{cm s}^{-2}$ )  $< 4.5$ ), which are appropriate for evolved K-type donors. The grid of synthetic spectra also contained models of different metallicities ( $[\text{Fe}/\text{H}]$ ). They were compared to the observed optical spectrum 54 (it is centred at phase 0.9822 and covers 0.975 to 0.99 orbital phases) and near-infrared (IR) photometry corrected for interstellar reddening.<sup>5</sup>

The observed data consist of two components,

- an optical spectrum obtained during the white dwarf eclipse, providing an uncontaminated view of the donor star and
- near-IR photometric points in the *JHK* bands, representing the donor’s long-wavelength emission, where the contribution from the disc and the white dwarf is not significant. However, we must remember that the IR data available through *Vizier* was most probably obtained outside of eclipse. Hence, it might exceed the IR tail of the SED in eclipse, simply because of the larger surface area of the RL-shaped donor star.

All model spectra were converted to physical flux units and scaled with the donor star’s radius as a free parameter. Each synthetic spectrum was convolved to the resolution of the observed data and scaled by the geometrical dilution factor  $(R/D)^2$ , where  $R$  is the radius of the donor and  $D$  is the distance to the system. The grid spanned distances

<sup>5</sup> Interstellar extinction was corrected assuming  $E(B - V) = 0.01$ , using the recalibration of the Cardelli et al. (1989) law by Fitzpatrick (1999), via the `dust_extinction` Python package.

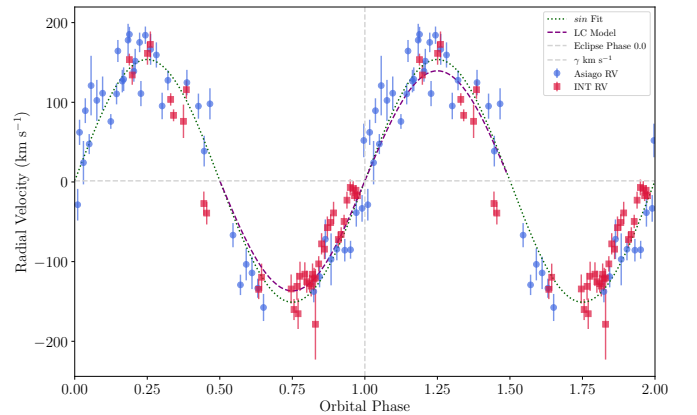


**Figure 6.** The measured RVs of the donor star from both sets of data, Asiago and INT, as marked in the legend. Corresponding RV curves are fits of a sinusoidal function to the separate data sets. The “model” RV curve was obtained by modelling the system parameters with light curves, as presented in Section 3.3.

from 1033 pc to 1073 pc, bracketing the Bailer-Jones et al. (2021)  $1\sigma$  uncertainty interval, which is our adopted distance range—and radii from 1.2 to 1.6  $R_{\odot}$ . The raw *Gaia* parallax distance of 1108 pc lies outside this range but is disfavoured by the probabilistic distance prior (see Section 2).

For each model, the reduced  $\chi^2$  statistic was computed over the optical spectral range (3500 to 10500 Å), comparing the model to the ISM-corrected observed flux. The IR photometric points were excluded from the  $\chi^2$  calculation because the archival IR data were most likely obtained outside eclipse and may reflect the larger projected emitting surface of the Roche-lobe-shaped donor; they were retained for qualitative consistency checks.

The best-fitting model corresponds to a BT-Settl atmosphere with  $T_{\text{eff}} = 4500$  K,  $\log g$  (cm s<sup>-2</sup>) = 4.0, and [Fe/H] = -0.5, scaled to a distance of 1053 pc and a donor star radius of 1.40 R<sub>⊙</sub>. The resulting spectrum, shown in the left panel of Fig. 5, provides the best match to the observed optical spectrum obtained during eclipse, when the contributions from the white dwarf and accretion disc are minimal, thus representing the donor star in its lowest observable emissivity state.

To validate the donor star spectral and luminosity class identification, we compare our best-fit model with a lower-resolution K3 IV template spectrum from Pickles (spectrum pickles\_uk\_59;  $T_{\text{eff}} = 4570$  K, 1998), shown in the left panel of Fig. 5.

To explore the fit sensitivity to stellar parameters and potential degeneracies, we plotted  $\chi^2$  as a function of effective temperature (right panel of Fig. 5). Each point in the diagram corresponds to a model with a specific  $T_{\text{eff}}$ ,  $\log g$ , and [Fe/H]. Points are colour-coded by metallicity and sized according to surface gravity (larger symbols represent lower  $\log g$ ). The diagram reveals a clear minimum around  $T_{\text{eff}} = 4500$  K and  $\log g$  (cm s<sup>-2</sup>) ≈ 4.0, with acceptable fits extending within ±100 K of the minimum.

This visualization not only identifies the best fit but also provides insight into the structure of the parameter space, illustrating how temperature and metallicity interact to shape the observed spectrum.

The apparent numerical differences between the temperatures derived from SED fitting ( $T_{\text{eff}} = 4500$  K) and the diagnostic diagram ( $T_{\text{eff}} = 4580$  K) reflect the finite resolution of the BT-Settl grid (100 K steps in  $T_{\text{eff}}$ , 0.5 dex steps in  $\log g$ ) rather than a genuine physical disagreement; any temperature in the range 4500 to 4650 K is an equally acceptable fit to the observed spectrum. The surface gravity is similarly constrained only to within the grid interval, and the best-fit  $\log g$  (cm s<sup>-2</sup>) = 4.0 should be understood as indicating an evolved, subgiant-like atmosphere rather than a precise measurement. Regarding metallicity, the available BT-Settl spectra cover only a discrete set of [Fe/H], so the best-fitting [Fe/H] = -0.5 is indicative rather than a definitive abundance determination; a proper measurement would require higher-resolution spectroscopy and a dedicated abundance analysis. We note that the MESA evolutionary models in Section 5 assume  $Z = 0.015$  (near-solar metallicity), which is required to reproduce the observed donor temperature and radius. This is nominally higher than the sub-solar metallicity suggested by the spectral fitting, but given the coarse [Fe/H] resolution of the BT-Settl grid and the absence of a dedicated abundance analysis, we do not consider this a significant inconsistency.

Using a complex of absorption lines in the  $\lambda\lambda$  5100–5500 Å range and a standard star template (HD165341, K0 V; Prugniel & Soubiran 2001), we measured the radial velocities (RVs) of the donor star from both the Asiago and INT observations. The RVs were determined by a cross-correlation method<sup>6</sup>. The orbital period derived from the RV variations agrees, within the uncertainties, with the photometric period, the latter being significantly more precise. The phase-folded

RV curves are shown in Fig. 6. A slight difference in the amplitude of the sinusoidal fits is observed between the two data sets. The combined result yields  $K_d = 151 \pm 10$  km s<sup>-1</sup>.

To constrain the donor mass, we employ the  $R_2$ – $M_2$  diagnostic diagram introduced by Tovmassian et al. (2025). The method combines the observed orbital period with the assumption that the donor star fills its Roche lobe. For a binary with a given orbital period, the Roche-lobe radius is uniquely determined by the masses of the two components through the binary separation and the mass ratio. Consequently, for each assumed white dwarf mass, one can calculate the Roche-lobe size as a function of the donor mass.

This produces a family of curves in the  $R_2$ – $M_2$  plane (Fig. 7 representing the radius that a Roche-lobe filling donor must have in a binary with the observed orbital period. Each curve corresponds to a different assumed white dwarf mass. The donor radius can be estimated independently from its brightness and effective temperature, with the Gaia distance. The Roche lobe filling donor star has a certain luminosity<sup>7</sup> for the distance determined by Gaia D = 1053<sup>+16</sup><sub>-19</sub> and given radius and  $T_{\text{eff}} = 4580$  K. These observational constraints appear in the diagram as a horizontal band corresponding to the allowed range of  $R_2$ . The light-shaded region in Fig. 7 encompasses the full range of donor radii consistent with the 1 $\sigma$  Gaia distance uncertainty (1033 to 1127 pc), and uncertainties related to the temperature and brightness of the donor star and its luminosity estimate.

The intersection between the observational radius constraint and the Roche-lobe curves provides the corresponding donor mass for each assumed white dwarf mass. In this way, the diagram allows us to visualize the allowed region of the  $R_2$ – $M_2$  parameter space and to determine the donor mass largely independently of the details of the light-curve modelling. According to Fig. 7 the donor mass is  $\approx 0.68^{+0.03}_{-0.07}$  M<sub>⊙</sub>. The tendency is toward lower mass, because the eclipse magnitude from ASAS-SN(V) is probably overestimated (ASAS-SN(V) ≈ ASAS-SN(g) – 0.3). Hence, the donor remains significantly undermassive relative to an isolated K3–K4 main-sequence star (Boyajian et al. 2012) across this entire range. The main conclusion is therefore robust against the distance uncertainty.

### 3.3 Light curve model

We used the  $g'$ -band and TESS light curve (LC) to apply a modelling tool developed by Zharikov et al. (2013), and described in detail in Subebekova et al. (2020) and Kára et al. (2021, 2023), to determine the system parameters and to study the structure of the accretion disc. The model consists of four components: the white dwarf, the donor star, the accretion disc, and the bright spot. Each component is represented by a set of triangles (projection) with certain  $T_{\text{eff}}$  projected along the line of sight. The model assumes that the disc radiates as a black body at the local effective temperature with radial distribution across the disc given by:

$$T_{\text{eff}}(r) = T_0 \left\{ \left( \frac{r}{R_{\text{WD}}} \right)^{-3} \left( 1 - \left[ \frac{R_{\text{WD}}}{r} \right]^{1/2} \right) \right\}^{\text{EXP}}, \quad (2)$$

$$T_0 = \left[ \frac{3G M_{\text{WD}} \dot{M}}{8\pi\sigma R_{\text{WD}}^3} \right]^{1/4},$$

where  $R_{\text{WD}}$  is the radius of the non-rotating helium WD (Nauenberg 1972),  $\dot{M}$  is the mass transfer rate, and  $\sigma$  is the Stefan–Boltzmann

<sup>6</sup> We used the xcsao task from the RVSAO package within IRAF (Kurtz & Mink 1998), which performs Fourier cross-correlation between object and template spectra.

<sup>7</sup> A bolometric correction BC = -0.395 was applied according to Montegriffo et al. (1998); Eker et al. (2020)

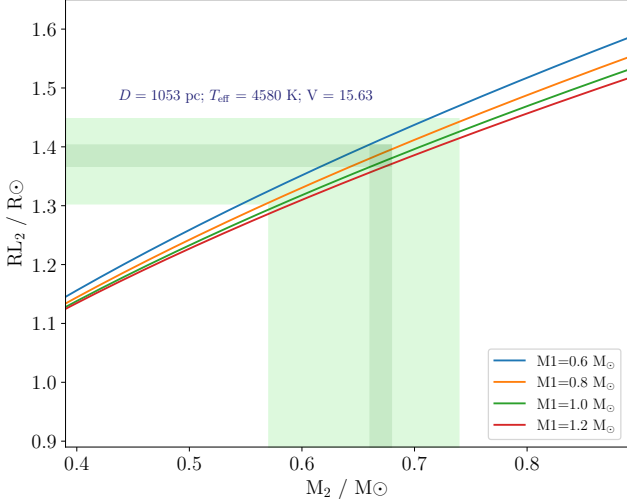


**Figure 7.** A diagnostic diagram of  $R_2 - M_2$  relation for SDSS J0852+7832 assuming that the donor star fills its Roche lobe and a spherical geometry. The light shaded area indicates the range of calculated radii of the donor stars in a full range of Gaia distances and the uncertainty of brightness estimates in the eclipse. The darker shaded area corresponds to  $T_{\text{eff}} = 4580$  K, yielding the observed luminosity of the donor star for the most probable distance of 1053 pc. A bolometric correction  $BC = -0.395$  and interstellar extinction  $E(B - V) = 0.01$  were applied to the estimated  $m_V = 15.63 \pm 0.1$  at the bottom of the eclipse to convert to the luminosity. The intersection of dark shaded areas indicates the preferred solution.

constant. In the standard accretion disc model, the radial temperature gradient is taken to be  $\text{EXP} = 0.25$  (Warner 1995, equation 2.35). We allow it to deviate slightly from this value, as in Linnell et al. (2010). The accretion disc thickness is defined as

$$z_d(r) = z_d(r_{\text{out}})(r/r_{\text{out}})^{\gamma_{\text{disc}}}, \quad (3)$$

where  $\gamma_{\text{disc}}$  is a free parameter for which we used the standard value of  $\gamma_{\text{disc}} = 9/8$  (Warner 1995, equation 2.51b) as the initial value. We also used the complex model for the hot spot, as described in detail by Kára et al. (2021, see their Fig. 9 and therein), where all parameter definitions can be found. The disc limb-darkening used in the model follows the Eddington approximation (Mayo et al. 1980; Paczynski & Schwarzenberg-Czerny 1980). The gravitational potential within the corresponding Roche lobe determines the shape of the stellar surface. The code includes the quadratic limb-darkening law for the primary and secondary with the limb-darkening coefficients taken from (Claret et al. 2012, 2013, 2020).

We fit the light curve by minimizing the  $\chi^2$  function, setting all parameters free, and using the gradient descent method to obtain self-consistent fit results. The best-fit parameters are given in Table 2 and the resulting light curves and the contribution of each component are presented in Fig. 8, left and right, respectively. The numbers in brackets for the variables in Table 2 are uncertainties defined as  $1\sigma$  of the Gaussian function approximation, which is used to describe the one-dimensional  $\chi^2$  function. The model predicts that in the  $g'$ -band, the light curve is formed by combining flux from two main components: the secondary and the disc. The contribution to the continuum from the hot spot and WD is significantly lower than theirs. The size of the accretion disc is expected to be the tidal truncation radius. For the derived mass ratio  $q = 0.82$ , the

**Table 2.** System parameters from the lightcurve modelling

<b>Fixed parameters:</b>	
$P_{\text{orb}}$	17.109 h
$E(B - V)$	0.01 mag.
Distance	1053.1 pc
$T_{\text{WD}}$	30000 K
<b>Variables of the LC fit:</b>	
Parameters of the system:	
$i$	$81.5^\circ(1.0)$
$M_{\text{WD}}$	$0.80(4) M_\odot$
$q = M_2/M_{\text{WD}}$	$0.82(9)$
$T_{2,\text{night}}$	$4700(100) \text{ K}$
$T_{2,\text{day,max},L_1}$	$5800^{+300}_{-600} \text{ K}$
$\dot{M} \times 10^{-8} M_\odot \text{ yr}^{-1}$	$7.1(8)$
Parameters of the disc:	
$R_{\text{d,in}}$	$\equiv R_{\text{WD}}$
$R_{\text{d,out}}$	$1.20^{+0.05}_{-0.2} R_\odot$
$h_{\text{d,out}}$	$0.150^{+0.025}_{-0.015} R_\odot$
<b>Calculated system parameters*:</b>	
$a$	$3.78 R_\odot$
$M_2$	$0.62 M_\odot$
$R_{2,x}$	$1.38 R_\odot$
$R_{2,y}$	$1.79 R_\odot$
$\log g_2$	$3.97$
$R_{\text{WD}}$	$0.01 R_\odot$
$\log g_1$	$8.36$

\* Those parameters correspond to the best fit. Numbers in brackets are uncertainties of variables.

tidal truncation radius is approximately 0.35–0.40 times the binary separation (e.g. Warner 1995), giving  $R_{\text{tid}} \approx 1.3\text{--}1.5 R_\odot$  for  $a = 3.78 R_\odot$ , consistent with the fitted value of  $R_{\text{d,out}} = 1.20^{+0.05}_{-0.2} R_\odot$ .

The geometry of the system is shown in Fig. 9 for a better understanding of the system and disc parameters. The colour bar in the figure indicates the effective temperature of the black body, corresponding to radiation from the system components.

### 3.4 Overall SED and the composition of the binary

In addition to optical spectral fitting, we constructed the full SED of the system, spanning from the UV to the mid-IR, and presented it in Fig. 10. The SED includes archival GALEX fluxes, our own Swift UVM2 measurement, optical spectroscopy during eclipse, and near-to mid-IR photometry. The plot also features the SDSS-V spectrum #53, obtained at the brightest orbital phase of 0.6. Using the best-fit parameters for the donor star ( $T_{\text{eff}} = 4500$  K,  $\log g = 4.0$ ), and the white dwarf parameters derived from light curve modelling ( $T_{\text{eff}} = 30,000$  K, consistent with the value adopted in Table 2,  $R_{\text{WD}} = 0.0099 R_\odot$ ), we generated a composite SED to compare it with the observed data. An unaccounted-for contribution from the accretion disc naturally explains the difference between the composite model and observations in the UV.

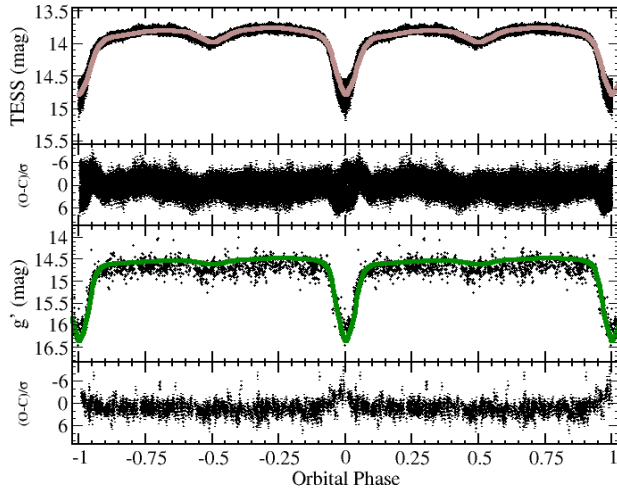


**Figure 8.** Light curve model fitting. In the left panel, the  $g'$ -band light curve of SDSS J0852+7832 is shown, along with the best-fit model in the upper panel. In the bottom panel,  $(O-C)/\sigma$  for data vs. model. In the right panel, the contributions of all components of the binary are presented to produce the modelled light curve.

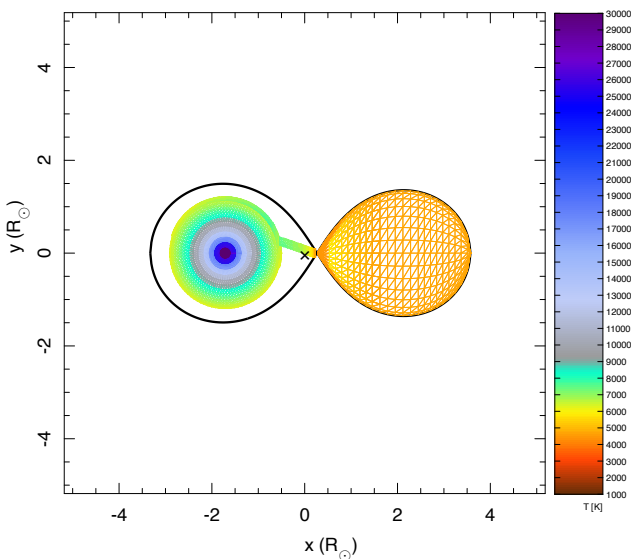


**Figure 9.** The composition of SDSS J0852+7832 corresponding to the best fit of the light curve. The axes show the dimensions of the components of the binary system in solar radii. Symbol “x” corresponds to the centre of mass.

The difference between the observed and model flux at the  $H$  band is approximately 20%. We do not know the orbital phases at which the IR data were obtained, but they were likely obtained outside eclipse. This discrepancy is due to the projected emitting surface of the donor star being much larger toward the back (toward the observer during eclipse) and toward its side, which qualitatively explains the observed infrared excess. Hence, multiplying the best-fit model by 1.25 improves the model’s fit to the IR data.

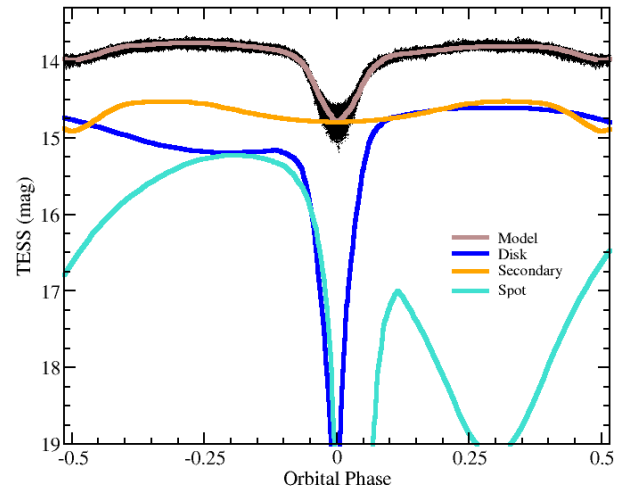


**Figure 10.** The SED of the SDSS J0852+7832 comprised of SDSS-V spectra taken in two epochs, one in the eclipse, the other around the maximum. Overplotted is the best-fit donor star model obtained from the grid of BT-Settl model atmospheres for Stars (Allard 2014), as in Fig. 7, but with a downgraded resolution for better illustration. To achieve a better fit of IR points (the dotted green line), it is sufficient to increase the radiating surface by a factor 1.25, which agrees with the Roche lobe projection ratio of  $R_{2,y}/R_{2,x}$  (see Table 2). We used a WD model from (Koester 2010) of  $T = 30,000$  K and  $\log g = 8.335$  (see text). The composite spectrum of the two stellar components is also shown, assuming that the contribution of the accretion disc to the continuum during the eclipse is negligible. In addition, the VizieR photometry of the object and the *Swift* (UVOT) measurement in the UVM2 band are plotted as points, all referenced in the legend. The fluxes in eclipse determined from the ASSASN are marked by crosses.

#### 4 EMISSION LINES AND CHARACTERISTICS OF THE ACCRETION DISC

The most direct evidence for disc emission in SDSS J0852+7832 comes from the eclipse morphology itself. During ingress, the near side of the rotating disc is progressively occulted, causing a sys-

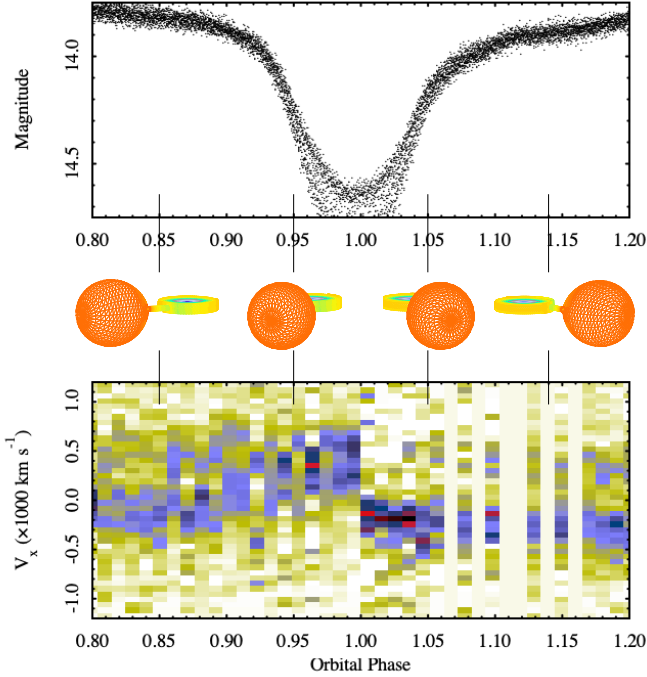


**Figure 11.** The eclipse morphology: In the upper panel, a portion of the TESS light curve around the eclipse is presented to be compared with the  $H\beta$  emission line behavior displayed in the form of a trailed spectrum in the bottom panel. An ingress and egress of the disc are embodied as a jump of red-shifted emission to the blue-shift in the trailed spectrum. In the middle, a cartoon of the binary system is shown in four orbital phases corresponding to 0.85, 0.95, 1.05, and 1.15. The binary system geometry is to scale.

tematic shift from red-shifted to blue-shifted emission; the reverse occurs during egress. This signature is clearly seen in the trailed spectrum of  $H\beta$  around the eclipse in Fig. 11, and is independently visible in He II, confirming that the disc contributes substantially to all major emission lines. The effect becomes more pronounced as the system brightness decreases during the partial eclipse, improving the line-to-continuum contrast.

Beyond the eclipse, the disc manifests as two parallel sine curves flanking the wings of He I,  $H\beta$ , and  $H\alpha$  in the trailed spectra (upper panel of Fig. 12), alongside the trailed spectra of the Fe I+Cr I absorption blend and the He II  $\lambda 4686$  emission line shown for comparison. The corresponding Doppler tomograms (see Marsh & Horne 1988; Marsh 2005) are given in the lower panels. The emission-line profiles are complex and suggest the presence of at least three kinematically distinct contributing regions, which in principle could be decomposed into three independent sinusoidal components. However, given the dominant and spatially extended disc contribution demonstrated by the eclipse morphology, such a decomposition would be highly degenerate and is not attempted here; the Doppler tomograms provide a more robust representation of the emitting geometry.

The first panels from the left show the Doppler map and trailed spectrum of the donor absorption line (inverted intensities), perfectly located within the Roche lobe contour. The following panels reveal double-peaked disc emission with additional components producing complex, line-dependent patterns. The disc emission peak is offset from exact counter-phase with the donor absorption by  $\phi \approx 0.071$ , corresponding to approximately 1.2 h in this 17 h system. This is a substantial and systematic phase shift rather than a minor asymmetry.

**Table 3.** Predicted and observed parameters of SDSS J0852+7832.

Parameter	Observed	Predicted
$P_{\text{orb}}$ (hr)	17.1094	17.1041
$R_2$ ( $R_{\odot}$ )	1.3 – 1.4	1.313
$M_2$ ( $M_{\odot}$ )	0.57 – 0.73	0.578
$T_{\text{eff},2}$ (K)	4550 – 4650	4638
$\log g_2$	4	3.964

It most plausibly arises from the combined effect of the bright spot at the stream–disc impact point and the non-axisymmetric disc structure induced by the mass-transfer stream, both of which are expected to produce a net phase offset of the integrated disc emission relative to the binary centre of mass (Marsh & Horne 1988). The most easily identifiable additional component is the low-velocity mass-transfer stream visible in  $H\alpha$ . A condensation in the third quadrant of the  $H\beta$  tomogram, present at lower intensity in all lines, is consistent with the stream–disc impact region. A further condensation in the first quadrant, partially outside the disc boundary, has no straightforward identification and may indicate stream overflow or a disc asymmetry; we refrain from further speculation given the complexity of the system. The strong He II emission line, originating in the innermost and hottest regions of the disc, produces a broad, centrally concentrated Doppler map with large velocity dispersion. Its trailed spectrum shows the same ingress red-to-blue shift pattern as the Balmer lines, providing additional confirmation that the inner disc is eclipsed.

## 5 EVOLUTION OF SDSS J0852+7832

We can use the parameters of the donor in SDSS J0852+7832 to search for reasonable evolutionary sequences that can explain its properties, following the steps we have already taken for V479 And and V1082 Sgr (Tovmassian et al. 2025). We used the MESA code (Paxton et al. 2011, 2013, 2015, 2018, 2019; Jermyn et al. 2023, r15140) to calculate binary evolution of the SDSS J0852+7832. As a result, we successfully found a reasonable model for SDSS J0852+7832, which is illustrated in Fig. 13. The properties we predict at the observed orbital period are in very reasonable agreement with the observed (Table 3), and our evolutionary sequence is summarized in Table 4. The model shows that Roche-lobe overflow begins at  $P_{\text{orb}} \approx 26.3$  h and the present-day configuration is reached  $\sim 4$  Myr later, during which the donor loses  $\sim 0.52 M_{\odot}$ . This corresponds to a mean mass-transfer rate of  $\sim 1.2 \times 10^{-7} M_{\odot} \text{ yr}^{-1}$  over this phase, declining to the current rate  $\dot{M} = 7.1(8) \times 10^{-8} M_{\odot} \text{ yr}^{-1}$  deduced from light curve modelling (Table 2), as the system settles towards a quasi-stable mass-transfer regime. A summary of the main assumptions is provided in what follows, but more details are found in Belloni & Schreiber (2023)<sup>8</sup> and Tovmassian et al. (2025).

The MESA equation of state is a blend of the OPAL (Rogers & Nayfonov 2002), SCVH (Saumon et al. 1995), FreeEOS (Irwin 2004), HELM (Timmer & Swesty 2000), PC (Potekhin & Chabrier 2010), and Skye (Jermyn et al. 2021) equations of state. Nuclear reaction rates are a combination of rates from NACRE (Angulo et al. 1999), JINA REACLIB (Cyburt et al. 2010), plus additional tabulated weak reaction rates (Fuller et al. 1985; Oda et al. 1994; Langanke & Martínez-Pinedo 2000). Screening is included via the prescription of

<sup>8</sup> <https://zenodo.org/records/8279474>

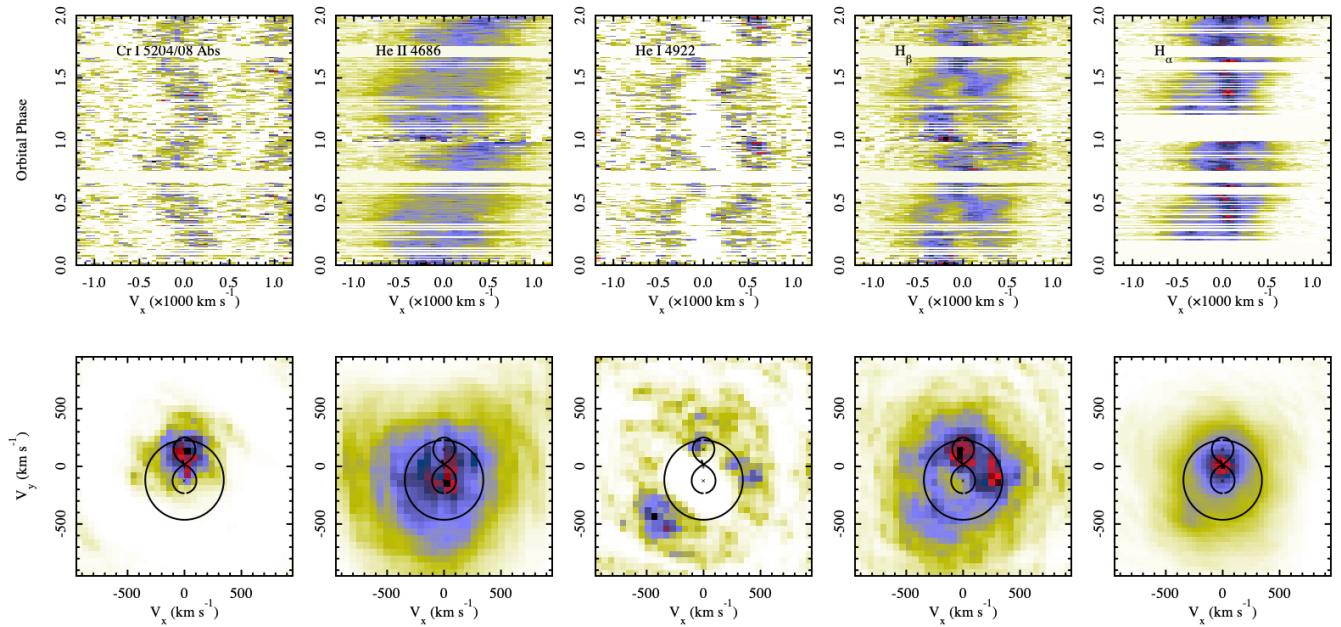


**Figure 12.** The trailed spectra of lines Fe I+Cr I in absorption, and emission lines He II, He I, H $\beta$ , and H $\alpha$  from left to right are presented in the upper panel. On the vertical axis, two orbital periods are plotted for illustration purposes. In the bottom panel, their corresponding Doppler tomograms are displayed. The description is in the text.

**Table 4.** Evolution of a zero-age post-CE binary towards the present-day properties of SDSS J0852+7832. The quantities  $M_1$  and  $M_2$  and Type $_1$  and Type $_2$  are the masses and stellar types of the progenitors of the WD and its companion, respectively.  $P_{\text{orb}}$  is the orbital period and the last column corresponds to the event occurring to the binary at the time in the first column. The row in which the binary has the present-day properties of SDSS J0852+7832 is highlighted in boldface.

Time (Myr)	$M_{\text{wd}}$ ( $M_{\odot}$ )	$M_2$ ( $M_{\odot}$ )	Type $_1$	Type $_2$	Orbital Period (h)	Event
0.0000	0.8	1.100	WD	main sequence	74.4000	initial post-common-envelope binary
5430.8294	0.8	1.098	WD	subgiant	74.4606	secondary becomes a subgiant
7114.3189	0.8	1.096	WD	subgiant	26.3389	onset of RL overflow
<b>7118.4898</b>	<b>0.8</b>	<b>0.578</b>	<b>WD</b>	<b>subgiant</b>	<b>17.1041</b>	<b>binary looks like SDSS J0852+7832</b>
7543.8066	0.8	0.165	WD	proto-WD	12.9063	end of RL overflow

Chugunov et al. (2007) and thermal neutrino loss rates are from Itoh et al. (1996). Electron conduction opacities are from Cassisi et al. (2007) and radiative opacities are primarily from OPAL (Iglesias & Rogers 1993, 1996), with a high-temperature Compton-scattering dominated regime calculated using the equations of Buchler & Yueh (1976). We assumed a metallicity of  $Z = 0.015$ , which is required to explain the low effective temperature and large radius of the donor star. We treated convective regions using the scheme by Henyey et al. (1965) for the mixing-length theory, adopting a mixing length of  $1.5 H_p$ , where  $H_p$  is the pressure scale height at the convective boundary. We assumed the grey Eddington  $T(\tau)$  relation to calculate the outer boundary conditions of the atmosphere (Paxton et al. 2011, their sect. 5.3). We adopted a uniform opacity that is iterated to be consistent with the final surface temperature and pressure at the base of the atmosphere. For low-temperature radiative opacities, we adopted the tables from Ferguson et al. (2005). We also used the nuclear network `cno_extras.net`, which accounts for the nuclear reactions of the carbon-nitrogen-oxygen-hydrogen burning cycle.

The main difference from our previous works is that we accounted for the impact of helium novae (Kato et al. 1989) on WD mass

growth. For hydrogen accretion, we included the critical accretion rates calculated by Wolf et al. (2013), as before. For helium accretion, i.e., the helium produced by stable hydrogen burning, we estimated the amount, which depends on the rate at which hydrogen is converted to helium, adopting the models from Kato & Hachisu (2004) and Wu et al. (2017). An essential ingredient in the simulations carried out by Belloni & Schreiber (2023) and Tovmassian et al. (2025), which is also incorporated here, is the use of the CARB model (Van & Ivanova 2019) to account for strong angular momentum loss via magnetic braking.

## 6 DISCUSSION

The long-period eclipsing binary SDSS J085210.48+783246.6 adds a new member to the small but growing family of cataclysmic variable-like systems with significantly evolved donor stars. The derived stellar and binary parameters — in particular, the 17.1 h orbital period, the K3 IV-type Roche-lobe-filling donor with  $M_2 = 0.6 \pm 0.1 M_{\odot}$  and  $R_2 \approx 1.4 R_{\odot}$ , and the presence of an accretion disc

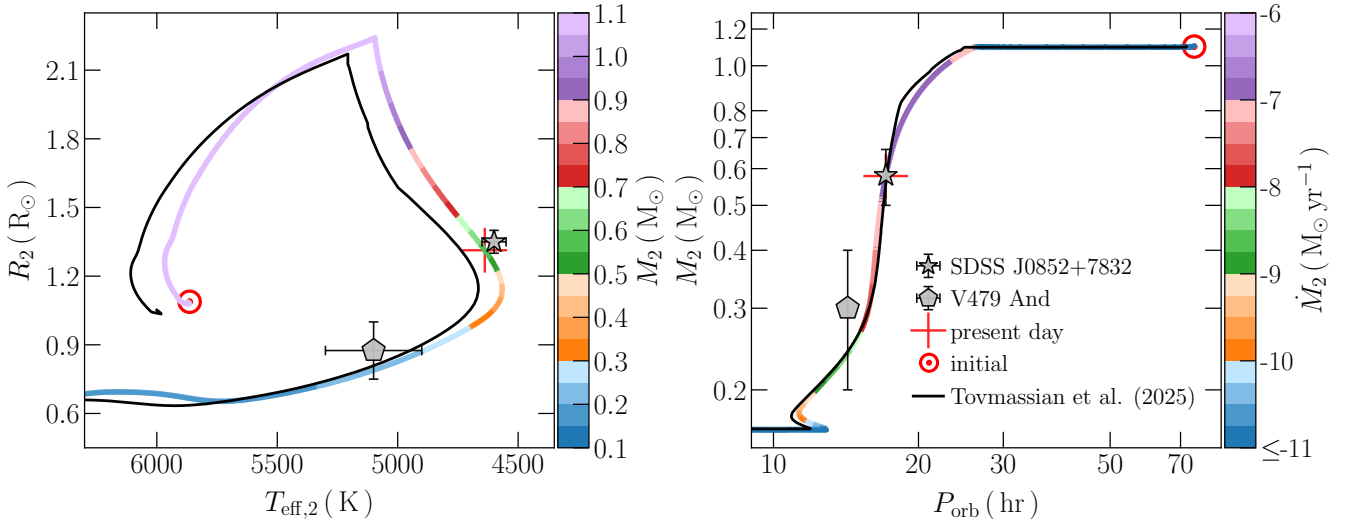


**Figure 13.** Post-CE evolution of the radius with the effective temperature of the donor in SDSS J0852+7832, colour-coded by its mass (left panel) and of the mass of the donor with the orbital period, colour-coded by the mass transfer rate (right panel). The red solar symbol indicates the properties at the moment the WD was formed (i.e., just after CE evolution), and the thick red cross indicates the properties at the moment the orbital period is the same as observed. The grey markers correspond to the properties derived from observations for SDSS J0852+7832 (star, this work) and V479 And (pentagon, [Tovmassian et al. 2025](#)).

(with a disc luminosity  $L_{\text{disc}} \sim GM_{\text{WD}}\dot{M}/R_{\text{WD}} \sim 4 \times 10^{32} \text{ erg s}^{-1}$ , comparable to the donor’s bolometric luminosity of  $\sim 3 \times 10^{32} \text{ erg s}^{-1}$  for  $T_{\text{eff}} = 4500 \text{ K}$  and  $R_2 \simeq 1.4 R_\odot$ ) around a  $\sim 0.8 M_\odot$  white dwarf — demonstrate that SDSS J0852+7832 is not a typical CV. Its donor star possesses a luminosity and temperature characteristic of a sub-giant, yet its mass is markedly lower than that of an isolated star of similar spectral type. This is a direct consequence of a previous phase of thermal-timescale mass transfer that stripped much of the donor envelope, after which the system settled into a quasi-stable mass-transfer regime characteristic of an advanced evolutionary stage.

The donor parameters inferred for SDSS J0852+7832 are supported by several independent approaches. The radius derived from the spectral energy distribution and Gaia distance is consistent with that required for a Roche-lobe-filling donor at the observed orbital period. The  $R_2$ – $M_2$  diagnostic diagram provides a graphical representation of this constraint by comparing the observed donor radius with the Roche-lobe size expected for a binary with the measured orbital period and different assumed white dwarf masses ([Tovmassian et al. 2025](#)). The intersection between these relations yields a donor mass of  $\sim 0.68^{+0.05}_{-0.11} M_\odot$ , in good agreement with the values obtained from light-curve modelling and from the evolutionary models.

It is noteworthy that the donor parameters derived from four independent methods — SED fitting, the  $R_2$ – $M_2$  diagnostic diagram, light curve modelling, and the MESA evolutionary models — are mutually consistent within their respective uncertainties (Tables 2 and 3). Despite relying on different assumptions and levels of model dependence, all approaches converge on a donor mass of  $\sim 0.6$ – $0.7 M_\odot$  and a radius of  $\sim 1.4 R_\odot$ . This consistency lends confidence to the overall characterization of the system despite the discrete nature of the model grids employed.

Our detailed modelling with MESA shows that SDSS J0852+7832 follows an evolutionary track similar to that of the long-period system V479 And ([Tovmassian et al. 2025](#)), differing mainly in being at an earlier point along that sequence. Both binaries are reproduced by post-common-envelope progenitors with comparable component masses under strong magnetic braking consistent with the CARB prescription of [Van & Ivanova \(2019\)](#). Within this frame-

work, SDSS J0852+7832 will naturally evolve towards a V479 And-like configuration as mass transfer continues and the orbital period shortens.

The two systems differ, however, in ways that underscore the diversity of outcomes within this evolutionary class. V479 And shows clear chemical abundance anomalies — including CNO-processed material at the surface — and observational signatures consistent with a synchronously rotating, strongly magnetized white dwarf ([Tovmassian et al. 2025](#)). The CNO surface anomalies in V479 And indicate that the donor’s convective envelope has dredged up material from layers previously processed by hydrogen burning, consistent with a more advanced stage of nuclear evolution than that inferred for SDSS J0852+7832. For SDSS J0852+7832, by contrast, we find no evidence for a strongly magnetized white dwarf: the emission-line profiles and Doppler tomograms are consistent with disc-dominated accretion in a non-magnetic nova-like system with a hot, flared disc ([Knigge et al. 2000](#)). These differences highlight the importance of detailed spectroscopic and magnetic diagnostics in characterizing long-period CVs with evolved donors.

What the present system does not yet tell us is where this sequence ultimately leads. The MESA models predict that SDSS J0852+7832 will continue losing mass and contract towards shorter orbital periods, eventually detaching once the hydrogen envelope is exhausted. The timescale on which the resulting binary subsequently evolves into a helium-transferring AM CVn system determines whether the system can be considered as representing progenitors of currently observed AM CVn systems. If the orbital period at detachment is short enough for gravitational-wave emission to drive the components back into contact within a Hubble time the latter would be the case.

However, our evolutionary track predicts detachment at  $P_{\text{orb}} \approx 12.9 \text{ h}$  (Table 4), which means that SDSS J0852+7832 is different from the progenitors of currently observed AM CVn systems, as the time to restart mass transfer exceeds a Hubble time. For the predicted component masses at detachment ( $M_{\text{WD}} \approx 0.8 M_\odot$ ,  $M_2 \approx 0.165 M_\odot$ ), the gravitational-wave merger timescale from  $P_{\text{orb}} \approx 12.9 \text{ h}$  is  $\tau_{\text{GW}} \sim G^3 M_1 M_2 (M_1 + M_2) / (48c^5 a^4) \sim 10^{12} \text{ yr}$  ([Belloni](#)

& Schreiber 2023), far exceeding the Hubble time. We therefore conclude that, while the predicted evolution of SDSS J0852+7832 resembles that predicted by Belloni & Schreiber (2023) for the formation of AM CVn, with respect to currently observed populations, SDSS J0852+7832 can be considered a progenitor of close double degenerate binaries.

What is established here is more immediate: the existence of a population of long-period, mass-transferring binaries with undermassive, nuclear-evolved donors that cannot be accommodated within the standard CV framework, and whose properties are naturally explained by strong magnetic braking acting on slightly evolved donors. Each new member of this class — SDSS J0852+7832, V479 And, V1082 Sgr — adds observational weight to the hypothesis that this channel is a significant, previously underestimated pathway in compact binary evolution.

## 7 CONCLUSIONS

SDSS J085210.48+783246.6 represents another example of a long-period interacting binary with a significantly evolved donor star. The system has an orbital period of 17.1 h and contains a K3 IV Roche-lobe-filling donor with  $M_2 \sim 0.6\text{--}0.7 M_\odot$  and  $R_2 \simeq 1.4 R_\odot$  transferring mass onto a  $\sim 0.8 M_\odot$  white dwarf.

The donor is markedly undermassive for its spectral type, indicating that it has undergone substantial envelope stripping during a previous phase of thermal-timescale mass transfer. The consistency between several independent parameter determinations — SED fitting, the  $R_2\text{--}M_2$  diagnostic diagram, light-curve modelling, and evolutionary modelling — provides a coherent picture of the system.

Evolutionary calculations suggest that SDSS J0852+7832 is presently at an earlier stage of the evolutionary sequence that includes systems such as V479 And. Together with V1082 Sgr and related objects, it supports the existence of a class of long-period CV-like binaries with evolved donors whose formation requires strong magnetic braking and significant prior nuclear evolution of the secondary star.

## ACKNOWLEDGEMENTS

GT was supported by grants IN109723 from the Programa de Apoyo a Proyectos de Investigación e Innovación Tecnológica (DGAPA-PAPIIT). DB acknowledges support from the São Paulo Research Foundation (FAPESP), Brazil, Process Numbers #2024/03736-2 and #2025/00817-4. SZh acknowledges grant IN105826, and JE was supported by grant IN113723, both from DGAPA-PAPIIT. This work is supported by the National Natural Science Foundation of China (NSFC, Nos. 12288102, 12125303), the Strategic Priority Research Program of the Chinese Academy of Sciences (grant Nos. XDB1160303, XDB1160300, XDB1160000, XDB1160200, XDB1160201), the CAS Project for Young Scientists in Basic Research (YSBR-148), the Yunnan Revitalization Talent Support Program “YunLing Scholar” project, International Centre of Supernovae (ICESUN), Yunnan Key Laboratory of Supernova Research (No. 202505AV340004), the New Cornerstone Science Foundation through the XPLOER PRIZE, and the Yunnan Revitalization Talent Support Program-Science & Technology Champion Project (No. 202305AB350003). We are grateful to Dr. U. Munari, who facilitated the observations at the Osservatorio Astrofisico di Asiago.

This paper includes data collected with the TESS mission, obtained from the MAST data archive at the Space Telescope Sci-

ence Institute (STScI). Funding for the TESS mission is provided by the NASA Explorer Program. STScI is operated by the Association of Universities for Research in Astronomy, Inc., under NASA contract NAS 5–26555. Funding for the Sloan Digital Sky Survey V has been provided by the Alfred P. Sloan Foundation, the Heising-Simons Foundation, the National Science Foundation, and the Participating Institutions. SDSS acknowledges support and resources from the Center for High-Performance Computing at the University of Utah. SDSS telescopes are located at Apache Point Observatory, funded by the Astrophysical Research Consortium and operated by New Mexico State University, and at Las Campanas Observatory, operated by the Carnegie Institution for Science. The SDSS website is [www.sdss.org](http://www.sdss.org). SDSS is managed by the Astrophysical Research Consortium for the Participating Institutions of the SDSS Collaboration, including the Carnegie Institution for Science, Chilean National Time Allocation Committee (CNTAC) ratified researchers, Caltech, the Gotham Participation Group, Harvard University, Heidelberg University, The Flatiron Institute, The Johns Hopkins University, L’Ecole polytechnique fédérale de Lausanne (EPFL), Leibniz-Institut für Astrophysik Potsdam (AIP), Max-Planck-Institut für Astronomie (MPIA Heidelberg), Max-Planck-Institut für Extraterrestrische Physik (MPE), Nanjing University, National Astronomical Observatories of China (NAOC), New Mexico State University, The Ohio State University, Pennsylvania State University, Smithsonian Astrophysical Observatory, Space Telescope Science Institute (STScI), the Stellar Astrophysics Participation Group, Universidad Nacional Autónoma de México, University of Arizona, University of Colorado Boulder, University of Illinois at Urbana-Champaign, University of Toronto, University of Utah, University of Virginia, Yale University, and Yunnan University.

Some/all of the data presented in this paper were obtained from the Multimission Archive at the Space Telescope Science Institute (MAST). STScI is operated by the Association of Universities for Research in Astronomy, Inc., under NASA contract NAS5-26555. Support for MAST for non-HST data is provided by the NASA Office of Space Science via grant NAG5-7584 and by other grants and contracts.

*Software and facilities:* This work made use of *ASTROPY* (Astropy Collaboration et al. 2013, 2018), *MESA* (Paxton et al. 2011, 2013, 2015, 2018, 2019; Jermyn et al. 2023, r15140), *PAMELA* and *MOLLY* (Marsh 1989), and *IRAF*. The following facilities were used: *Gaia*, SDSS V, *Swift* (XRT and UVOT), TESS, ZTF, ASAS-SN, ATLAS, ING 2.5 m (INT/IDS), and Asiago 1.22 m.

## DATA AVAILABILITY

The data analysed in this work can be made available upon reasonable request to the authors.

## REFERENCES

- Allard F., 2014, in Booth M., Matthews B. C., Graham J. R., eds, IAU Symposium Vol. 299, Exploring the Formation and Evolution of Planetary Systems, pp 271–272, doi:10.1017/S1743921313008545
- Álvarez-Hernández A., et al., 2021, *MNRAS*, 507, 5805
- Angulo C., et al., 1999, *Nuclear Physics A*, 656, 3
- Aros-Bunster C., et al., 2025, *A&A*, 693, L11
- Astropy Collaboration et al., 2013, *A&A*, 558, A33
- Astropy Collaboration et al., 2018, *AJ*, 156, 123

- Bailer-Jones C. A. L., Rybizki J., Fouesneau M., Demleitner M., Andrae R., 2021, *AJ*, **161**, 147
- Barnes S. A., Sofia S., 1996, *ApJ*, **462**, 746
- Barraza-Jorquera J. A., Schreiber M. R., Belloni D., 2025, *A&A*, **696**, A92
- Bellm E. C., et al., 2019, *PASP*, **131**, 018002
- Belloni D., Schreiber M. R., 2023, *A&A*, **678**, A34
- Belloni D., Schreiber M. R., Moe M., El-Badry K., Shen K. J., 2024, *A&A*, **682**, A33
- Belloni D., Schreiber M. R., El-Badry K., 2025, *A&A*, **697**, A100
- Boyajian T. S., et al., 2012, *ApJ*, **757**, 112
- Buchler J. R., Yueh W. R., 1976, *ApJ*, **210**, 440
- Burrows D. N., et al., 2000, in X-Ray and Gamma-Ray Instrumentation for Astronomy XI. pp 64–75
- Burrows D. N., et al., 2005, *Space Science Reviews*, **120**, 165
- Capaldi M., Perri M., Saija B., Tamburelli F., 2005, The Swift XRT Data Reduction Guide, Version 1.2. NASA/GSFC & HEASARC, [https://swift.gsfc.nasa.gov/analysis/xrt\\_swguide\\_v1\\_2.pdf](https://swift.gsfc.nasa.gov/analysis/xrt_swguide_v1_2.pdf)
- Cardelli J. A., Clayton G. C., Mathis J. S., 1989, *ApJ*, **345**, 245
- Cassisi S., Potekhin A. Y., Pietrinferni A., Catelan M., Salaris M., 2007, *ApJ*, **661**, 1094
- Chugunov A. I., Dewitt H. E., Yakovlev D. G., 2007, *Phys. Rev. D*, **76**, 025028
- Claret A., Hauschildt P. H., Witte S., 2012, *A&A*, **546**, A14
- Claret A., Hauschildt P. H., Witte S., 2013, *A&A*, **552**, A16
- Claret A., Cukanovaite E., Burdge K., Tremblay P.-E., Parsons S., Marsh T. R., 2020, *A&A*, **634**, A93
- Cyburtt R. H., et al., 2010, *ApJS*, **189**, 240
- Eker Z., et al., 2020, *Monthly Notices of the Royal Astronomical Society*, **496**, 3887
- El-Badry K., Rix H.-W., Quataert E., Kupfer T., Shen K. J., 2021, *MNRAS*, **508**, 4106
- Ferguson J. W., Alexander D. R., Allard F., Barman T., Bodnarik J. G., Hauschildt P. H., Hefner-Wong A., Tamanai A., 2005, *ApJ*, **623**, 585
- Fitzpatrick E. L., 1999, *PASP*, **111**, 63
- Flewelling H. A., et al., 2020, *The Astrophysical Journal Supplement Series*, **251**, 7
- Fuller G. M., Fowler W. A., Newman M. J., 1985, *ApJ*, **293**, 1
- Gaia Collaboration et al., 2023, *A&A*, **674**, A1
- Gehrels N., et al., 2004, *ApJ*, **611**, 1005
- Godet O., et al., 2009, *Astronomy & Astrophysics*, **494**, 775
- Guidry J. A., et al., 2021, *ApJ*, **912**, 125
- HI4PI Collaboration 2016, *Astronomy & Astrophysics*, **594**, A116
- Heinze A. N., et al., 2018, *AJ*, **156**, 241
- Henyey L., Vardya M. S., Bodenheimer P., 1965, *ApJ*, **142**, 841
- Iglesias C. A., Rogers F. J., 1993, *ApJ*, **412**, 752
- Iglesias C. A., Rogers F. J., 1996, *ApJ*, **464**, 943
- Irwin A. W., 2004, The FreeEOS Code for Calculating the Equation of State for Stellar Interiors, <http://freeeos.sourceforge.net/>
- Itoh N., Hayashi H., Nishikawa A., Kohyama Y., 1996, *ApJS*, **102**, 411
- Jenkins J. M., et al., 2016, in Chiozzi G., Guzman J. C., eds, Society of Photo-Optical Instrumentation Engineers (SPIE) Conference Series Vol. 9913, Software and Cyberinfrastructure for Astronomy IV. p. 99133E, [doi:10.1117/12.2233418](https://doi.org/10.1117/12.2233418)
- Jermyn A. S., Schwab J., Bauer E., Timmes F. X., Potekhin A. Y., 2021, *ApJ*, **913**, 72
- Jermyn A. S., et al., 2023, *ApJS*, **265**, 15
- Kára J., Zharikov S., Wolf M., Kučáková H., Cagaš P., Medina Rodriguez A. L., Mašek M., 2021, *A&A*, **652**, A49
- Kára J., Zharikov S., Wolf M., Amantayeva A., Subebekova G., Khokhlov S., Agishev A., Merc J., 2023, *ApJ*, **950**, 47
- Kato M., Hachisu I., 2004, *ApJ*, **613**, L129
- Kato M., Saio H., Hachisu I., 1989, *ApJ*, **340**, 509
- Knigge C., Long K. S., Hoard D. W., Szkody P., Dhillon V. S., 2000, *The Astrophysical Journal*, **539**, L49
- Knigge C., Baraffe I., Patterson J., 2011, *ApJS*, **194**, 28
- Kochanek C. S., et al., 2017, *Publications of the Astronomical Society of the Pacific*, **129**, 104502
- Koester D., 2010, *Mem. Soc. Astron. Italiana*, **81**, 921
- Kurtz M. J., Mink D. J., 1998, *Publications of the Astronomical Society of the Pacific*, **110**, 934–977
- Langanke K., Martínez-Pinedo G., 2000, *Nuclear Physics A*, **673**, 481
- Linnell A. P., Godon P., Hubeny I., Sion E. M., Szkody P., 2010, *ApJ*, **719**, 271
- Marsh T. R., 1989, *PASP*, **101**, 1032
- Marsh T. R., 2005, *Ap&SS*, **296**, 403
- Marsh T. R., Horne K., 1988, *MNRAS*, **235**, 269
- Matt S. P., et al., 2015, *ApJ*, **799**, L23
- Mayo S. K., Wickramasinghe D. T., Whelan J. A. J., 1980, *MNRAS*, **193**, 793
- Montegriffo P., Ferraro F. R., Origlia L., Fusi Pecci F., 1998, *Monthly Notices of the Royal Astronomical Society*, **297**, 872
- Nauenberg M., 1972, *ApJ*, **175**, 417
- Oda T., Hino M., Muto K., Takahara M., Sato K., 1994, *Atomic Data and Nuclear Data Tables*, **56**, 231
- Paczynski B., Schwarzenberg-Czerny A., 1980, *Acta Astron.*, **30**, 127
- Paxton B., Bildsten L., Dotter A., Herwig F., Lesaffre P., Timmes F., 2011, *ApJS*, **192**, 3
- Paxton B., et al., 2013, *ApJS*, **208**, 4
- Paxton B., et al., 2015, *ApJS*, **220**, 15
- Paxton B., et al., 2018, *ApJS*, **234**, 34
- Paxton B., et al., 2019, *ApJS*, **243**, 10
- Pickles A. J., 1998, *PASP*, **110**, 863
- Potekhin A. Y., Chabrier G., 2010, *Contributions to Plasma Physics*, **50**, 82
- Prugniel P., Soubiran C., 2001, *A&A*, **369**, 1048
- Rappaport S., Verbunt F., Joss P. C., 1983, *ApJ*, **275**, 713
- Reiners A., Mohanty S., 2012, *ApJ*, **746**, 43
- Ricker G. R., et al., 2015, *Journal of Astronomical Telescopes, Instruments, and Systems*, **1**, 014003
- Ritter H., Kolb U., 2003, *A&A*, **404**, 301
- Rogers F. J., Nayfonov A., 2002, *ApJ*, **576**, 1064
- Roming P. W. A., et al., 2005, *Space Sci. Rev.*, **120**, 95
- Sarkar A., Ge H., Tout C. A., 2023a, *MNRAS*, **519**, 2567
- Sarkar A., Ge H., Tout C. A., 2023b, *MNRAS*, **520**, 3187
- Saumon D., Chabrier G., van Horn H. M., 1995, *ApJS*, **99**, 713
- Shappee B. J., et al., 2014, *ApJ*, **788**, 48
- Skumanich A., 1972, *ApJ*, **171**, 565
- Smee S. A., et al., 2013, *The Astronomical Journal*, **146**, 32
- Subebekova G., Zharikov S., Tovmassian G., Neustroev V., Wolf M., Hernandez M. S., Kučáková H., Khokhlov S., 2020, *MNRAS*, **497**, 1475
- Szkody P., et al., 2011, *AJ*, **142**, 181
- Timmes F. X., Swesty F. D., 2000, *ApJS*, **126**, 501
- Tovmassian G., et al., 2025, *A&A*, **703**, A119
- UK Swift Science Data Centre 2023, XRT Analysis Threads: Introduction to XSELECT, <https://www.swift.ac.uk/analysis/xrt/xselect.php>
- Van K. X., Ivanova N., 2019, *ApJ*, **886**, L31
- Warner B., 1995, Cataclysmic variable stars. Vol. 28, Cambridge University Press
- Wolf W. M., Bildsten L., Brooks J., Paxton B., 2013, *ApJ*, **777**, 136
- Wu C., Wang B., Liu D., Han Z., 2017, *A&A*, **604**, A31
- Zharikov S., Tovmassian G., Aviles A., Michel R., Gonzalez-Buitrago D., García-Díaz M. T., 2013, *A&A*, **549**, A77

This paper has been typeset from a  $\text{\TeX}/\text{\LaTeX}$  file prepared by the author.